Quantitative Spectral/Spatial Analysis of Phased Array Coil in Magnetic Resonance Imaging Based on Method of Moment

Fa-Hsuan Lin, Wei-Peng Kuan, Shyh-Kang Jeng, and Jyh-Horng Chen*

***Abstract*—A new approach for analysis of RF coils in magnetic resonance (MR) experiments is reported. Instead of assuming current distribution in conventional quasi-static algorithm, this approach transforms the coil geometry into an equivalent circuit for complex current calculation. Self and mutual inductance are taken into consideration. Frequency responses of RF coils and transverse magnetic field (B_1) maps can be simulated. This approach is especially efficient for phased array coil design for its small matrix size when implemented on computers. Experiments on both single surface coil and phased array coils are consistent with simulation results.**

***Index Terms*—Magnetic resonance, method of moment, phased array coil, RF coil.**

I. Introduction

PHASED array coils [1] were first proposed for its high signal-to-noise-ratio (SNR) and large field-of-view (FOV) magnetic resonance (MR) imaging. It combines both the advantages of surface coils and volume coils and has been applied to physiological or anatomical investigation [2], [3]. In designing phased array coils, the most important issue is the minimization of mutual inductance among different ports of the coil [1]. Such minimization is usually achieved by appropriately overlapping neighboring surface coils.

Conventionally, the quasi-static simulation approach based on Biot–Savart's law [4] is widely adopted for verification of the coil design. However, this method fails for phased array because of its limitation in mutual inductance evaluation. Besides, the quasi-static approach assumes a current distribution on the coils and thus fails when coils are used in high-field imaging. Although there are some other approaches, such as the finite element method [5] or the finite difference time domain (FDTD) [6] method, they require major computation for satisfactory results in general.

Manuscript received February 19, 1998; revised July 30, 1999. The Associate Editor responsible for coordinating the review of this paper and recommending its publication was M. Vannier. *Asterisk indicates corresponding author.*

F.-H. Lin is with the Program of Medical Engineering and Medical Physics, Harvard University, Cambridge, MA 02138 USA, and with the Division of Health Science and Technology, Massachusetts Institute of Technology, Cambridge, MA 02139 USA.

S.-K. Jeng and *J.-H. Chen are with the Department of Electrical Engineering, National Taiwan University, Taipei, Taiwan, R.O.C.

W.-P. Kuan is with the Department of Biotechnology, National Yang-Ming University, Taipei, Taiwan, R.O.C.

Publisher Item Identifier S 0278-0062(99)10407-5.

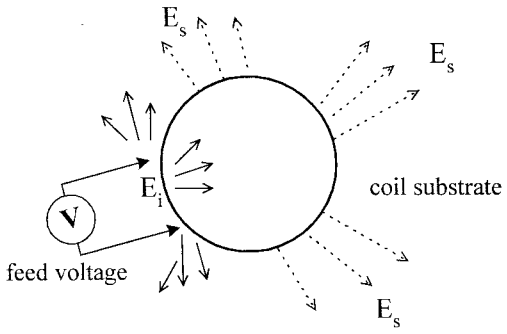

Fig. 1. Scattering due to a coil for an incident electric field from impressed voltage source. The established incident electric field comes from the impressed voltage source. To satisfy the boundary conditions for the perfect electric conductor where no tangential electric field exists, a scattered electric field must be built.

Here we report a new simulation approach based on the method of moment [7]. This method takes all time-harmonic electromagnetic wave properties into account. It assumes no current distribution and provides both the frequency responses of coil and B_1 field map.

II. Theory and Method

The Problem of Electric Field Scattering

As the voltage source was applied on the coil, it is equivalent to setting up an incident electrical field $\vec{E}_i$, as shown in Fig. 1. Due to the boundary condition of zero tangential electrical field on perfect electric conductor, the scattered field $\vec{E}_s$ is generated to satisfy

$$[\vec{E}_s + \vec{E}_i]_{\text{tangential}} = 0. \tag{1}$$

From Maxwell equations, the scattered field can be expressed as

$$\vec{E}_s(\vec{J}) = -jw\vec{A} - \nabla\Phi \tag{2}$$

where $\vec{A}$ and Φ are the magnetic vector potential and electric scalar potential, respectively. They can be given as

$$\vec{A}(\vec{r}) = \frac{\mu}{4\pi}\int_v \frac{J(\vec{r'})\cdot e^{-jk|\vec{r}-\vec{r'}|}}{|\vec{r}-\vec{r'}|}\,dv \tag{3}$$

$$\Phi(\vec{r}) = \frac{1}{4\pi\varepsilon}\int_v \frac{\sigma(\vec{r'})\cdot e^{-jk|\vec{r}-\vec{r'}|}}{|\vec{r}-\vec{r'}|}\,dv \tag{4}$$

where $\vec{J}(\vec{r}')$ and $\rho(\vec{r}')$ are the induced current and charge on the surface of the coil. Note that $k = w\sqrt{\mu\varepsilon}$ is the wave number, w is the operating frequency, and μ and ε are the permeability and the permittivity of free space.

If the conductor strips of the coil are quite thin and narrow, we can replace the volume source integral into a surface integral or even a line integral. The charge source and the current distributions are related by the conservation of charge

$$\sigma(\vec{r}) = -\frac{\nabla \cdot \vec{J}(\vec{r})}{jw}. \tag{5}$$

Equation (1) then becomes an integral equation after we substitute (2)–(5) in it.

III. Method of Moment

In this study we use the method of moment [7] to solve the electrical field integral equation above. The method of moment can be divided into two parts. First, the current on the coil is decomposed into a linear combination of basis functions, where the basis functions can be chosen according to the physical properties of the scattering body or mathematical convenience. Second, we approximate for each basis function coefficient.

For convenience, the loop pulse functions

$$\overline{P_n}(\vec{r}) = \begin{cases} 1 \cdot \hat{c}, & \text{for } \vec{r} \text{on the coil strip, where } \hat{c} \text{ is the} \\ & \text{unit vector along the surface of the coil} \\ 0, & \text{otherwise} \end{cases} \tag{6}$$

are adopted as basis functions, i.e.,

$$\vec{J} = \sum_{n=1}^{N} In \cdot \vec{P}_n(\vec{r}). \tag{7}$$

P_n is the loop pulse function for loop n and I_n is the coefficient of the loop pulse function P_n.

The inner product of two functions was defined as

$$\langle \vec{f} \cdot \vec{g} \rangle = \int_L \vec{f} \cdot \vec{g}\, ds \tag{8}$$

where the integral path L is along one loop of the coil. Now let us take the inner products on both sides of the integral equation, we have

$$\langle \overline{E_i}, \overline{P_n}(\overline{r}) \rangle = jw \langle \overline{A}, \overline{P_n}(\overline{r}) \rangle + \langle \nabla\Phi, \overline{P_n}(\overline{r}) \rangle, \quad n = 1, 2, \cdots, N. \tag{9}$$

The second term of the above equation can be evaluated as

$$\begin{aligned} \langle \nabla\Phi, \overline{p_n}(\overline{r}) \rangle &= \int_L \nabla\Phi \cdot \overline{p_n}(\overline{r})\, dl \\ &= \int_L (\nabla \cdot \Phi \overline{p_n}(\overline{r}))\, dl = 0 \end{aligned} \tag{10}$$

where we have applied the divergence of a loop pulse basis function.

The divergence of a loop pulse basis function is

$$\nabla \cdot \overline{P_n}(\overline{r}) = \begin{cases} \pm\delta(\overline{r}), & \text{at the boundary of the loop} \\ 0, & \text{otherwise.} \end{cases} \tag{11}$$

The electric field integral equation then becomes

$$\left\langle \left| \begin{matrix} \vec{A} \\ \vec{E} \end{matrix} \right|, \vec{P}_n(\vec{r}) \right\rangle = \int_L \left| \begin{matrix} \vec{A} \\ \vec{E} \end{matrix} \right| \cdot d\vec{l}. \tag{12}$$

The incident electric field term can be written as

$$\langle \vec{E}_i, \vec{P}_n(\vec{r}) \rangle = V_n. \tag{13}$$

This represents a voltage drop across the testing loop due to the impressed voltage source.

Matrix Equation

The matrix equation (9) is in the form of

$$[Z] \cdot [I] = [V] \tag{14}$$

where $[Z]$ is the impedance matrix of entries. The entry Z_{mn} in the impedance matrix

$$Z_{mn} = jw \int_{\text{loop } m} \overline{A_n} \cdot \bar{\hat{c}}_m\, dl_m, \quad \text{where } \bar{\hat{c}}_m \text{ is the unit} \cdot \text{vecto } r \text{ along the loop } m \tag{15}$$

$$\overline{A_n} = \frac{\mu}{4\pi} \int_v \frac{e^{jk|\overline{r_m} 0 \overline{r_n}|}}{|\overline{r_m} - \overline{r_n}|} \cdot dv_n \tag{16}$$

represents the voltage drop along loop m for a unit-intensity current on basis n. Since the impedance matrix is a full matrix, it includes the mutual inductance effects.

If the width of each conductor strip is negligible comparing to the size of the coil, then the volume integral can be simplified as a line integral. In our experiments, the lengths of coils are about 20–55 cm, and the width of the coil strips are less than 1.0 cm. Thus we approximate

$$\overline{A_n} = \frac{\mu}{4\pi} \int_{l_m} \frac{e^{-jk|\overline{r_m} - \overline{r_n}|}}{|\overline{r_m} - \overline{r_n}|} \cdot \bar{\hat{c}}_m\, dl_m. \tag{17}$$

Impedance Calculation

To simplify the calculation, we decompose the coils into linear combinations of straight conductors. The nondiagonal entries of the impedance matrix can be approximated, as shown in Fig. 2

$$Z_{mn} = \frac{jw\mu}{4\pi} \int_{lm} \int_{ln} \frac{e^{-jkr_{mn}}}{r_{mn}}\, d\, ln \cdot dlm[\bar{\hat{c}}_n \cdot \bar{\hat{c}}_m] \text{ where } r_{mn} = |\overline{r_m} - \overline{r_n}|. \tag{18}$$

In real cases, the product of the wave number and the coil geometrical size is small. For example, a 15-cm-diameter coil in a 1.5-T scanner makes this product about 0.33. If we utilize Taylor's approximation to expand the exponential in (18), we find that taking four leading terms is sufficient.

After the approximation we have

$$\begin{aligned} Z_{mn} &\approx \frac{jw\mu}{4\pi}[\vec{c}_n \cdot \vec{c}_m] \\ &\quad \cdot \int_{lm} \int_{ln} \frac{1 - jkr_{mn} - \frac{1}{2}k^2 r_{mn}^2 + \frac{1}{6}jk^3 r_{mn}^3}{r_{mn}}\, dl_m\, d_{ln} \\ &= \frac{jw\mu}{4\pi}[\vec{c}_n \cdot \vec{c}_m] \cdot \{I_1 + I_2 + I_3 + I_4\}. \end{aligned} \tag{19}$$

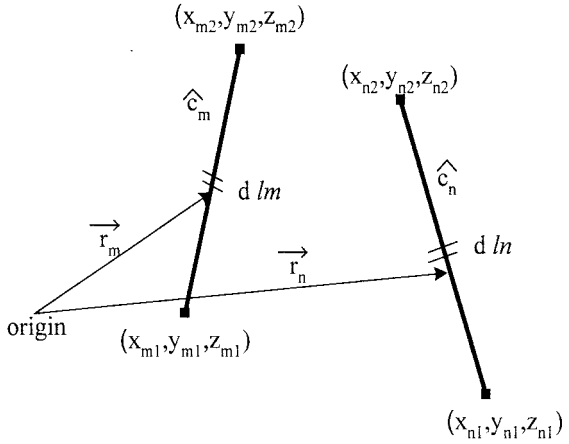

Fig. 2. Spatial coordinates and parameters for calculation of mutual inductance between two distinct linear current segment. As segments making up the coil are separated much larger than their widths, we can neglect the finite widths of these segments by approximation of linear segments.

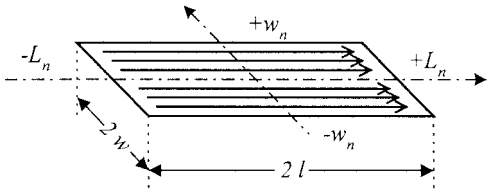

Fig. 3. Geometrical parameters for calculation of self inductance. During calculation of self-induction the width of coil segment cannot be neglected. We must include the effects of finite width of the coil segment to cancel the singularity from the line current approximation.

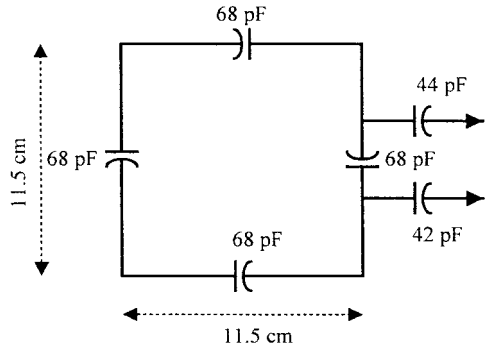

Fig. 4. The size and electric parameters of the square surface coil. The width of the conductor strips making up the coil is 0.5 cm.

These four integrals, I_1, I_2, I_3, and I_4 can be further simplified. The coordinates of two pulses are depicted in Fig. 2.

For self-inductance entry, the approximation (19) is not applicable, and we must replace the line integral by the planar integral

$$Z_{mn} = \frac{j\omega\mu}{4\pi} \int_{l_n^-}^{l_n^+} \int_{l_n^-}^{l_n^+} \int_{w_n^-}^{w_n^+} \frac{e^{-jk|\vec{r}|}}{2W_n|\vec{r}|}\, dw_n\, d;_n\, dl_n \quad (20)$$

where w_n is the width of the coil strip and l_n is the length of the coil strip, as shown in Fig. 3.

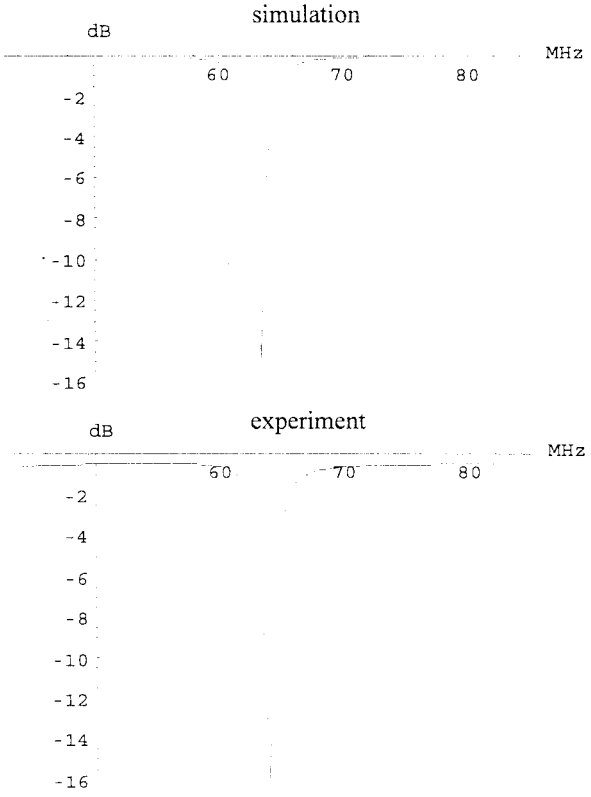

Fig. 5. Simulated frequency response of a single square surface coil and that measured from network analyzer. Frequency responses are reflection coefficients measured and simulated. Central frequency, 3-dB bandwidth, and maximal reflection coefficient are all quite matched.

We also approximate the exponential term by the first four terms of Taylor expansion to obtain

$$\begin{aligned} Z_{nm} \approx & \frac{j\omega\mu}{4\pi} \\ & \cdot \int_{l_n^-}^{l_n^+} \int_{l_n^-}^{l_n^+} \int_{w_n^-}^{w_n^+} \\ & \cdot \frac{1 - jk|\vec{r}| - \frac{1}{2}k^2|\vec{r}|^2 + \frac{1}{6}jk^3|\vec{r}|^3}{2W_n \cdot |\vec{r}|}\, dw_n\, dl_n\, dl_n \\ = & \frac{j\omega\mu}{4\pi} \cdot (I_{s1} + I_{s2} + I_{s3} + I_{s4}). \end{aligned} \quad (21)$$

Excitation of Coil

The voltage matrix is an N by 1 matrix where N is the number of current bases. Generally, there is only one port connected to the analog-digital-converter (ADC) and/or post preamplifier of the MR scanner. Thus, the voltage matrix is a vector with only one nonzero entry. Due to the fact that the proposed scattering model is a linear system, we can use the superposition theorem to calculate the response due to several sources when there is more than one voltage source.

This proposed model could be applied for coils as either transmitters or receivers, because of reciprocity.

Frequency Response and B_1 Field Map

After we obtain the complex current on the coil, the spectrum of the RF coil could be calculated by power reflection

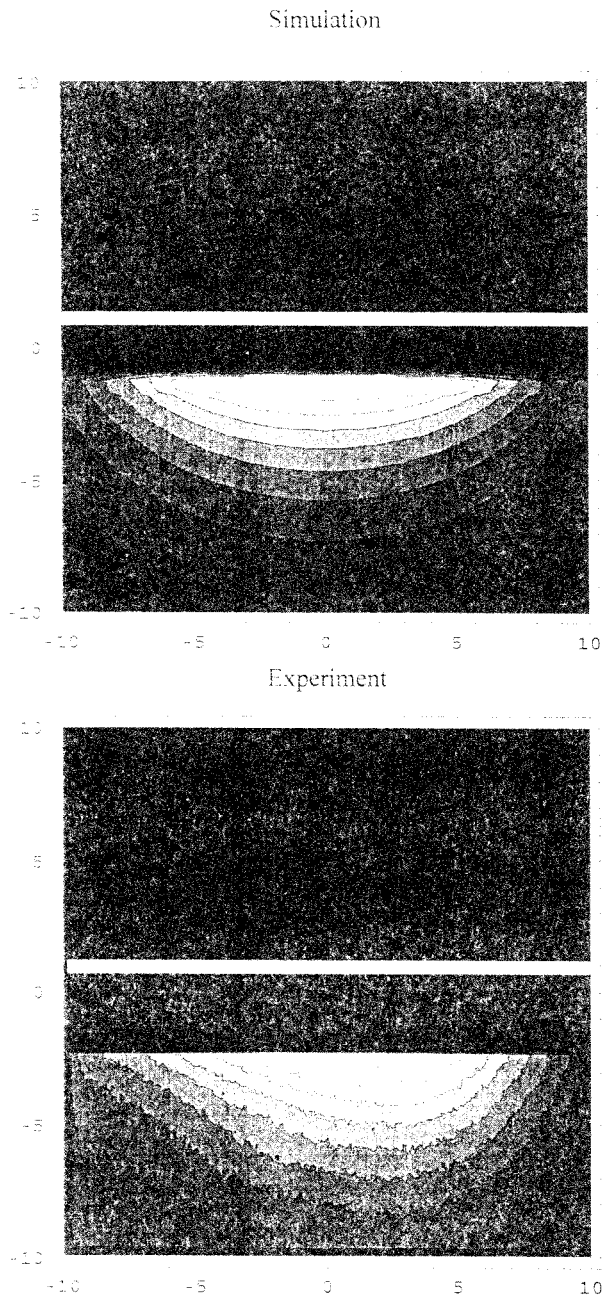

Fig. 6. The phantom images of axial slice from simulation and experiment. These images are normalized between zero and one. The white bars represent the spatial position of the surface coils. The B_1 field maps were linearly normalized between zero and one. Contours are the results of the linearly segmented ten gray levels of the field strength.

coefficients at different frequencies

$$\Gamma = \frac{Z_{in} - Z_0}{Z_{in} + Z_0}. \tag{22}$$

Z_{in} is the input impedance of the RF coil and Z_0 is the characteristic impedance of the transmission line. Input impedance is defined as the ratio of impressed voltage over the input current at the feeding point of the voltage source.

With an explicit complex current we can also derive the time harmonic magnetic field B_1 at any point. This is derived

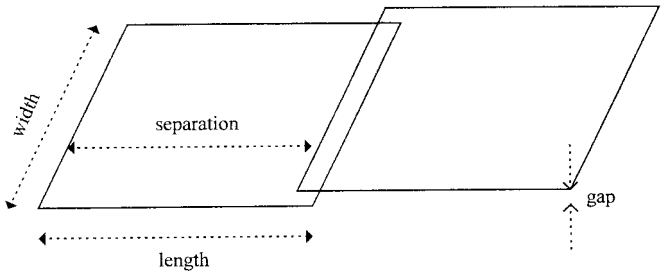

Fig. 7. The mesh of the two-channel phased array coil.

from vector potential and Maxwell equations.

$$\vec{A} = \sum_{\text{all the current}} \int_{v'} \frac{\vec{J}(\vec{r}) e^{-jk|\vec{r}-\vec{r}'|}}{4\pi|\vec{r}-\vec{r}'|}\, dv'$$
$$\vec{B} = \nabla \times \vec{A}. \tag{23}$$

IV. Materials

All the simulations were implemented on a Sun Sparc 20 Workstation. The programs were written in ANSI C language. The 20-point Gaussian quadrature numerical integration was adopted for the one-dimensional (1-D) integration. The matrix inversion was completed via the LU decomposition method [8].

Coils were designed for a 1.5-T scanner, which corresponds to the Larmor frequency at 63.87 MHz. Coils were fabricated by 99.9999% copper substrate. Capacitors from American Technical Ceramics and Johanson are utilized for coil tuning and matching. Experiments were performed on a General Electric Signa 1.5-T scanner. The frequency response of the reflection coefficient in decibels was measured by a Hewlett Packard 8751A network analyzer.

A single square surface coil and a two-channel phased array coil were produced to verify the model. The two-channel phased array consisted of two single square coils. Furthermore, we have extended this algorithm for the head phased array coil design of four-channel, six-channel, and eight-channel cases, respectively.

V. Results

A. Single Square Surface Coil

The size and electric components for the square surface coils are depicted in Fig. 4. To make the surface coil as reception only, we used a pin diode in series with an additional inductor as a shunt path in the resonant circuit as the switch, a widely adopted circuit configuration, to decouple in the RF transmission. The width of the conductor strips is 0.5 cm. The frequency responses of surface coils from simulation and the network analyzer are shown in Fig. 5. Since the surface coil is reception only, we used the body coil as the RF transmitter. The same scheme was used in the following array experiments. The axial slice of B_1 field mapping is shown in Fig. 6. These images are normalized between zero and one. The white bars represent the spatial position of the surface coils. The B_1 field

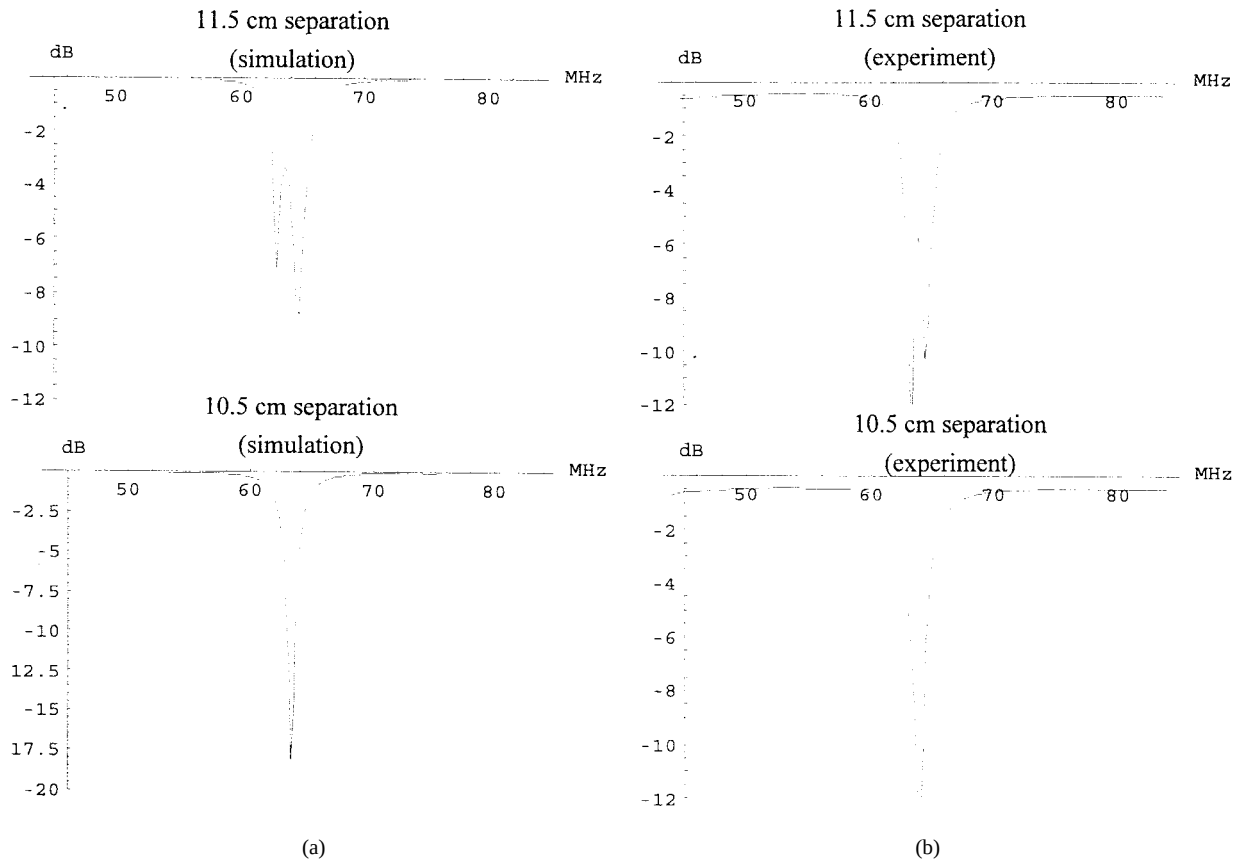

Fig. 8. (a) Simulated frequency response of two-channel phased array coil at different separations. (b) Frequency response of two-channel phased coil measured from network analyzer at different separations.

maps were linearly normalized between zero and one. Contours are the results of the linearly segmented ten gray levels of the field strength. The axial slice is aligned with the isocenter of the scanner. The FOV is 20 cm * 20 cm. The image was required acquired by a spin-echo sequence (TR = 500 ms, TE = 20 ms, NEX = 1). The simulation results predicted successfully the intensity contours as compared with the experimental results. Around the center of the surface coil there was a higher magnetic field. And the magnetic field is weaker as the field points away from the coil plane and the center of the coil. The axial slice from the experiment is noisier and slightly asymmetric compared to the simulation, which may be due to the fact that no average excitation was applied (only one NEX).

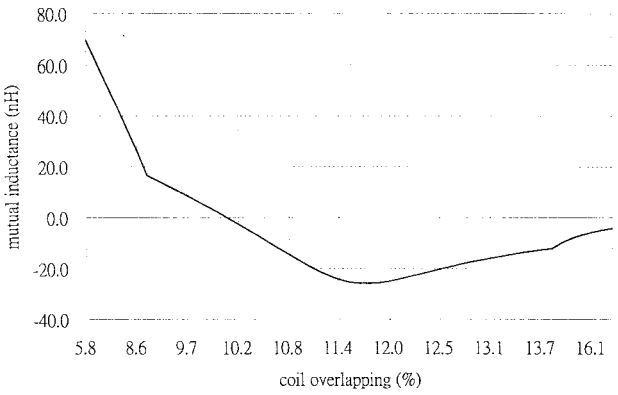

Fig. 9. Variation of mutual inductance between two square surface coil at different separations between coils.

B. Two-Channel Phased Array Coil

To eliminate the mutual inductance interference between two coils in this array, a different separation distance between coils were tested. The mesh of this two-port phased array coil is shown in Fig. 7. Each of the surface coils has identical geometry, as described in Fig. 4. The definition of overlapping ratio for the planar phased array is the percentage ratio of overlap, which is the difference of coil length and coil separation, over length, as shown in Fig. 7. The simulated and experimental frequency responses corresponding to different separations are shown in Fig. 8(a) and (b). In simulation, two peaks of the frequency response merged as the separation reached 10.5 cm. The experiment result assures the evaluation of mutual inductance as a function of coil separation. Two separated peaks of frequency response (11.5-cm separation) merged into a single peak as separation changed to 10.5 cm in the experiment, as predicted in the simulation.

Fig. 9 shows the simulated mutual inductance as a function of coil overlapping in percentages. At an overlapping ratio of 10%, i.e., 10.35-cm separation (side length is 11.5 cm), the mutual inductance approaches zero. This separation (10.35 cm) is quite close to the result from the simulated frequency response [10.5 cm in Fig. 8(a) and (b)]. The polarity of the mutual inductance means nothing but the polarity of the induced voltage.

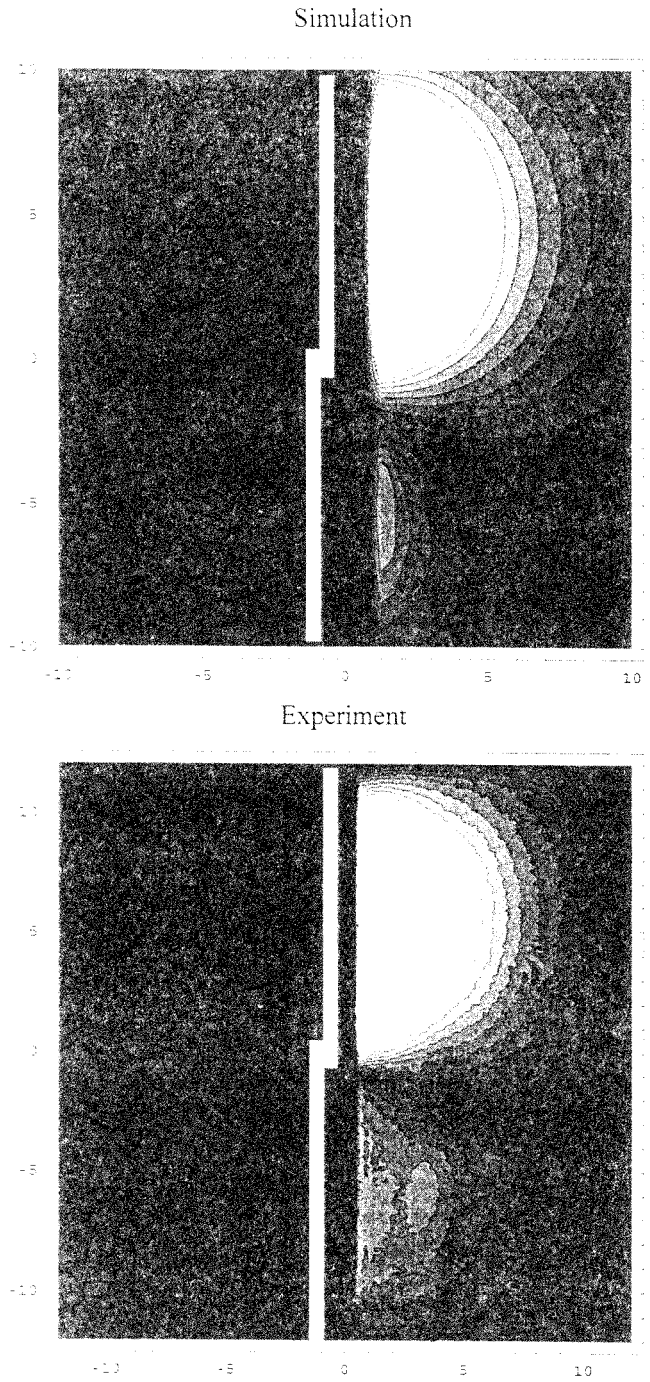

Fig. 10. Phantom images of a sagital slice for the two-channel phased array coil from simulation and experiment. The white bars represent the spatial position of the two surface coils.

The B_1 field map from a phantom is shown in Fig. 10. The predicted sensitivity depth for this array, about 5 cm, matches the experiment result. There is a noisy sensitive region at the lower part of the experiment image, which may come from the extraction circuit located on the imaging slice. The gradient of the sensitive region is matched. The experiment image is acquired by the spin-echo sequence (TR/TE 500/20, 1 NEX).

In Fig. 11, we show the optimal overlapping ratio, which is defined as the percentage ratio of overlapping distance over length of rectangle coil corresponding to the different coil

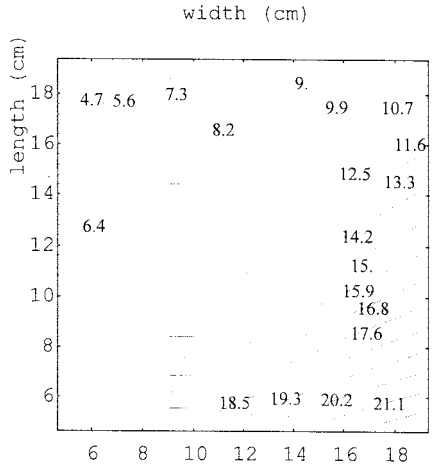

Fig. 11. Contour plot of the optimal planar overlapping ratio.

width. The width and the length range from 5 cm to 19 cm. The gap between the two surface coils is 0.5 cm. The labels in the figure are a percentage planar overlapping ratio to cancel the mutual inductance. At optimal overlap, the mutual inductance between the coils was cancelled.

C. Head Phased Array Coil of Four-Channel, Six-Channel and Eight-Channel Cases

The optimized overlapping ratio for a volume phased array coil for head imaging is presented here. An example mesh of a six-channel head phased array is depicted in Fig. 12.

The frequency responses from four- and eight-channel head phased arrays are shown in Fig. 13(a) and (b). A small peak in the four-channel simulated spectrum comes from the induction of opposite array element, because the two face-to-face loop coils have a larger mutual inductance. This mutual inductance cannot be cancelled via overlapping. The measured spectrum is noisy because of imperfection in fabrication. Given the coil dimension, individual geometry, and overlapping conditions, simulation still predicts precisely the central frequency and the single peak of the frequency response. The combined phantom image from simulation and experiments is depicted in Fig. 14. We can observe the signal-sensitive region around the periphery of the phased array, because this location is close to the surface of the curved element surface coil. The central region is less signal sensitive due to the larger distance between the surface of curved element surface coil.

To quantify the overlap between neighboring coils in a phased array, we define the volume overlap ratio as the percentage of the extra arc length over the average arc length. The average arc length is defined as the arc length of one element in the array if we divide the cylinder into identical elements. Extra arc length is the overlapping arc segment length. The overlap ratio for different numbers of channels with different radius heights is shown in Figs. 15 and 16. In Fig. 15, the optimal volume overlap ratio for a 12-cm radius head phased array as a function of height for four, six, and eight channels is shown. The gap is 1 cm. If the phased array height is increased, its overlap ratio is higher. While there are more channels which correspond to smaller curved

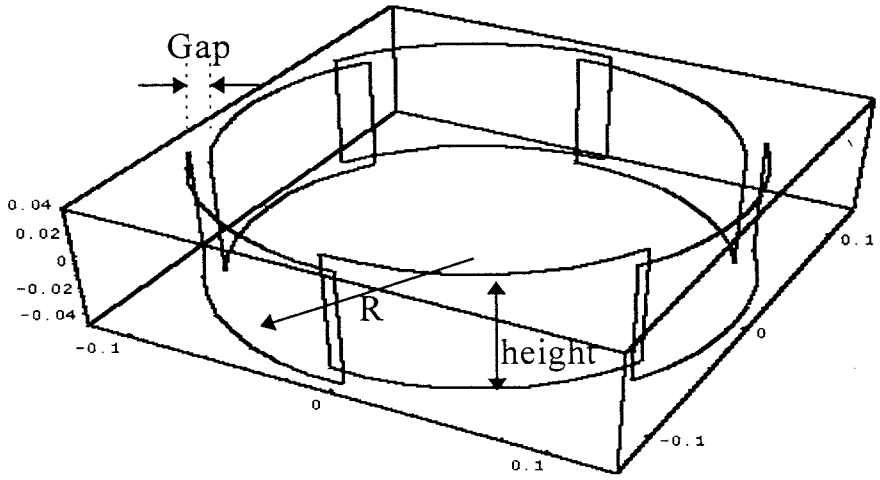

Fig. 12. Mesh of a six-channel head phased array coil. Each curved planar coil overlaps two neighboring coils to cancel the mutual inductance.

element coils, the overlap ratio is also higher. Fig. 16 depicts the optimal volume overlap ratio for a 10-cm height phased array as a function of radius for four, six, and eight channels with a gap of 1 cm. As the radius is increased, less overlap is required. Fewer channels require a lower overlap ratio.

VI. Discussion

The advantage of the dc simulation approach is its simplicity in computation and explicitness in physical meaning. With the given current distribution on the coil mesh, designers can easily get the B_1 field map. The disadvantage of the dc model lies in the requirement of assigning a current distribution on the coils, which is even more difficult for high-frequency coils and complicated geometry. Another disadvantage of the dc model is the defection in spectral analysis, which is important in developing feasible coils for both coil tuning and matching.

By our proposed ac model based on the method of moment, we do not have to assume the current distribution on the coil. Designers only provide the geometrical definition of the coil mesh and the excitation condition. The impedance matrix entries, which are related to the operating frequency, coil geometry, and current are calculated directly. The currents calculated by the ac model are complex numbers, which include phase information for further B_1 field map and coil frequency responses. The complex current is necessary for coil design in high field scanners, for the wavelength in high field scanner is relatively short. From the calculated complex current we can derive both the spatial B_1 map and spectrum. The disadvantage of the ac model is the longer simulation time than the dc model. The bottleneck is in the manipulation of the impedance matrix inversion, which is necessary for current calculation. In spectral domain analysis, hundreds of matrix inversions are required for current calculation at different frequencies. However, by using the suggested loop current basis functions and testing functions, the dimension of the impedance matrix is small and the simulation is very efficient. For example, the simulation of a two-channel planar phased array is completed within 5 s. The frequency response consisting of 200 points for an eight-channel head phased array is obtained within 10 s.

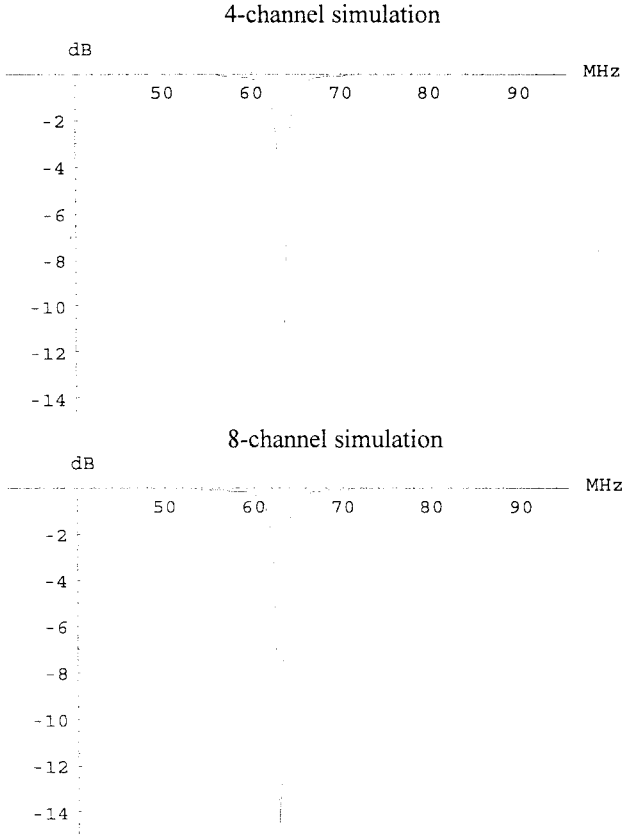

Fig. 13. (Top) Simulated frequency response for the four- and eight-channel head phased array coils. The frequency response is the reflection coefficient of the coil. (Bottom) Frequency response of the four- and eight-channel head phased array coil measured from the network analyzer. The frequency response is the reflection coefficient of the coil. These results are noisier due to imperfection of coil fabrication.

It is much faster than the finite element of finite-difference-time-domain numerical simulation schemes.

Our proposed simulation procedures have less computation load because of the benefits of the loop testing function (10). Here, for simplicity, we also used the loop function as the current basis. However, we could use other bases, such as the

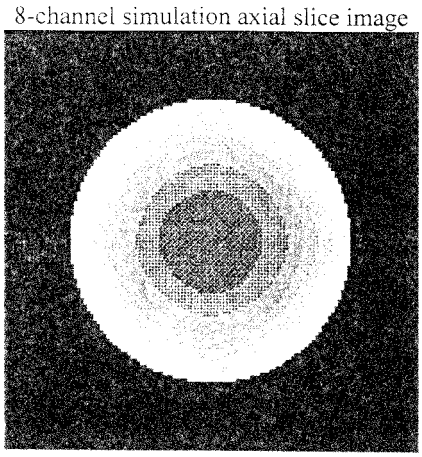

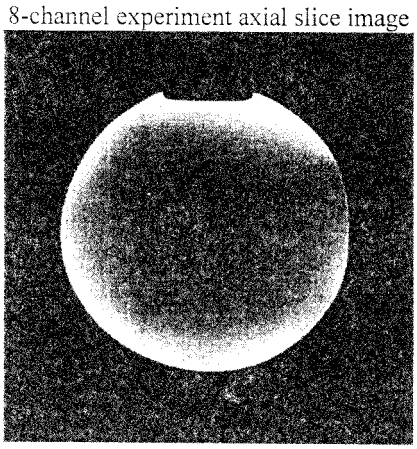

Fig. 14. Phantom image of the axial slice from a combination of all ports of the eight-channel head phased array coil.

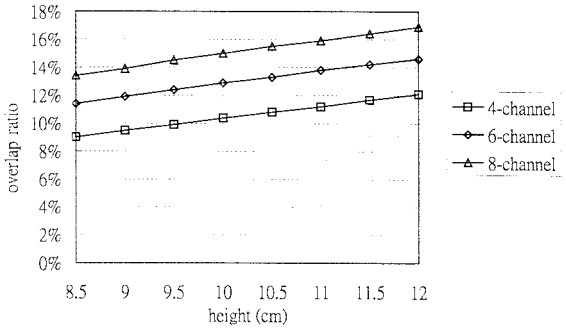

Fig. 15. Optimal volume overlap ratio for the 12-cm-radius head phased array at different height and different number of ports.

pulse basis, in simulation. Changing the basis makes the matrix dimension larger and therefore increases the computation time. However, we could investigate the effects of locations of capacitors if we adopt the pulse current basis and loop testing function at the same time. Although the matrix dimension is larger, we could minimize the computation by dropping one term by the loop basis (10).

From the simulation of a single square surface coil, we get satisfactory matches between simulation and experimental

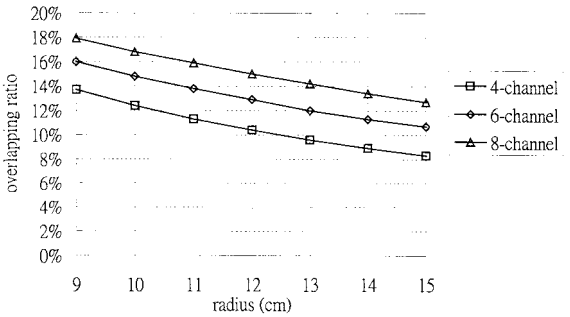

Fig. 16. Optimal volume overlap ratio for a 10-cm-height head phased array at different radius and different number of ports.

results. Some errors of the simulation may derive from the imperfection of coil production. Three slices of images from simulation and experiments are consistent. The localized high-sensitivity region from the MR scanner may come from the asymmetry of the signal extraction circuit. To make it easier to connect the coil and ADC channel of the scanner, an extraction circuit is placed at the right-hand side of the coil. Such a placement spoils the symmetry of the coil and affects the uniformity of the loop basis function. Other designs concerning the placement of the extraction circuit can avoid this asymmetry.

In the analysis of a two-channel phased array coil we can visualize the phenomenon of mutual inductance cancellation at specific coordinates. Deviation from this specific coordinate will introduce mutual inductance, which spoils the single peak in the spectrum. Traditionally, this mutual inductance is understood qualitatively. With the aid of this new simulation approach we can quantify this mutual inductance. Comparing the sagittal slices from the dc and ac models, we can see that the AC model's results are closer to the experimental results, as shown in Fig. 17. Some residual mutual impedance is found due to signal propagation between adjacent channels. This can be observed at the lower part of the image from the experiment. The ac model based on the method of moment includes such a mutual inductance effect and predicts better than the dc model. This minor mutual inductance cannot be observed obviously in the frequency response of B_1 maps by the ac model. In addition, the current on the single surface coil must be identical along the coil with value calculated directly from the coil geometry, which is proved by the gradient of the B_1 field map. The gradient of the simulation based on method of moment predicts better the result than the dc simulation.

Overlap ratios of different geometries for the volume phased array coil are illustrated in Figs. 15 and 16. They are verified via the isolation between neighboring coils from B_1 field maps at appropriate slices. The isolation of the implemented array can be verified from the B_1 field map. There is no apparent signal coupling other than the single element itself. Fig. 17 gives an example. The isolation between elements can also be verified by the spectrum. The quasi-single-peak spectrum at Fig. 13(b) is another example.

Another deficiency of this proposed model is the lack of simulation for loading, which is the next focus of this study. And, due to the simplicity of the loop basis function in phased array, the performance due to the different positions of the

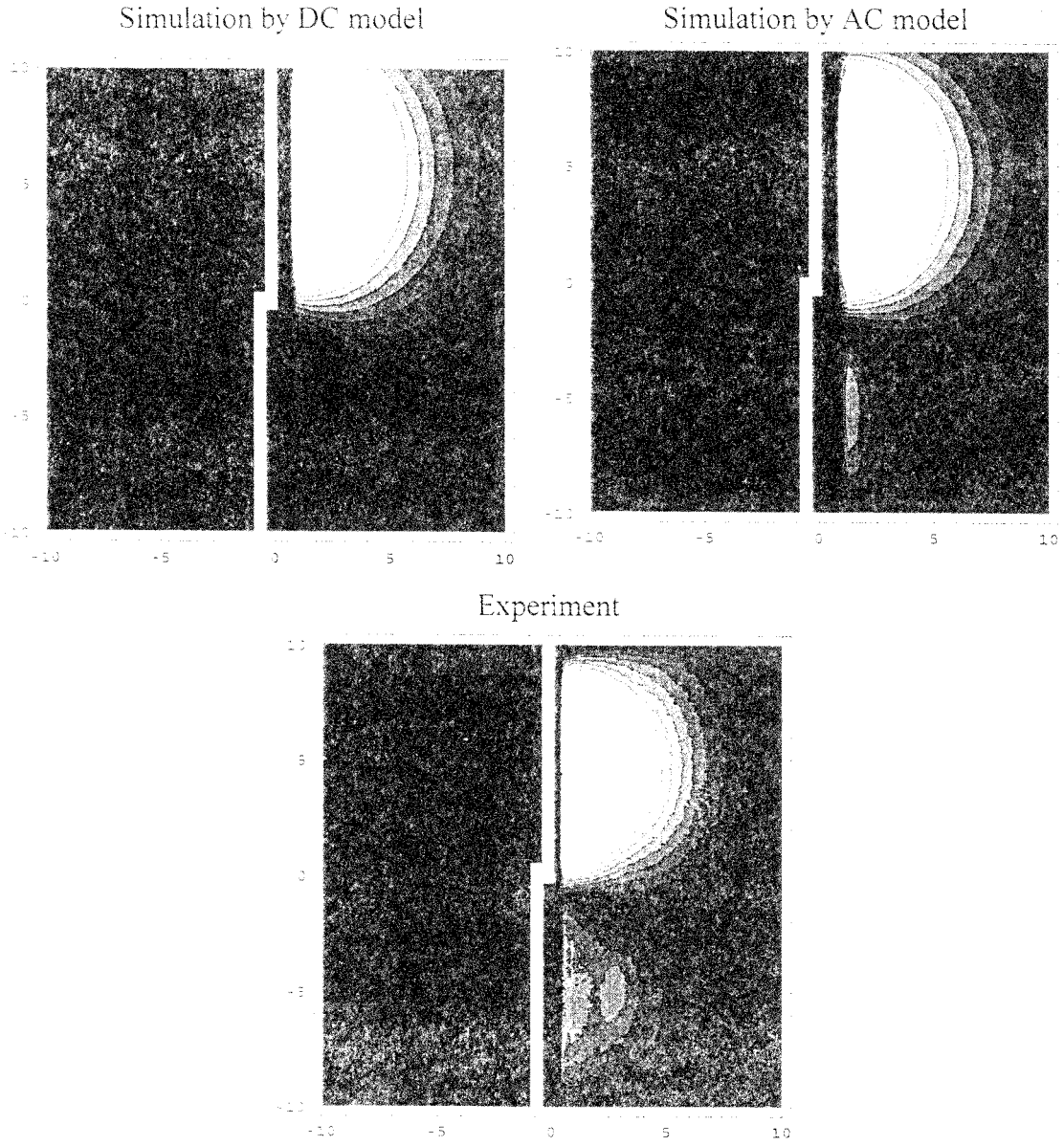

Fig. 17. Comparison of a sagittal slice image of a two-channel phased array coil from the quasi-static simulation approach, method of moment scheme, and experimental result. The white bars represent the spatial position of two surface coils.

capacitors cannot be evaluated. This may be improved by using other basis functions.

VII. Conclusion

We have proposed a model for analysis of RF coils in magnetic resonance experiments. This algorithm is especially efficient for a phased array coil. Phased array coils with arbitrary geometry can be analyzed by this method. Instead of assuming current distribution on the coil in a conventional quasi-static simulation scheme, our model transforms the coil mesh into an equivalent circuit and calculates the complex current distribution on the coil. Performances of coils including frequency responses and B_1 maps have been evaluated. Self/mutual inductance of the phased array have also been taken into consideration. Optimized overlapping ratios for volume phased array design with verification have been reported. Further works will concentrate on the application of this simulation approach for optimization of RF coils and loading effects.

References

[1] P. B. Roemer, W. A. Edelstein, C. E. Hayes, S. P. Souza, and O. M. Mueller, "The NMR phased array," *Magn. Reson. Med.*, vol. 16, pp. 192–225, 1990.

[2] C. D. Constantinides, C. R. Westgate, W. G. O'Dell, E. A. Zerhouni, and E. R. McVeigh, "A phased array coil for human cardiac imaging," *Magn. Reson. Med.*, vol. 34, pp. 92–98, 1995.

[3] L. L. Wald, L. Carvajal, S. E. Moyher, S. J. Nelson, P. E. Grant, A. J. Barkovich, and D. B. Vigneron, "Phased array detectors and an automated intensity-correction algorithm for high-resolution MR imaging of the human brain," *Magn. Reson. Med.*, vol. 34, pp. 433–439, 1995.

[4] W. T. Sobol, "Dedicated coils in magnetic resonance imaging," *Rev. Magn. Reson. Med.*, vol. 1, no. 2, pp. 181–224, 1986.

[5] L. S. Petropoulos, E. M. Haacke, R. W. Brown, and E. Boerner, "Predicting RF field penetration in heterogeneous bodies using a 3-D finite element approach: Preliminary results," *Magn. Reson. Med.*, vol. 30, p. 366, 1993.

[6] W. L. Ko, "Analyzes of RF coils in MRI by FD-TD," in *Proc. Annu. Conf. Engineering Medicine Biology*, 1991, vol. 13, pt. 1.

[7] R. F. Harrington, *Field Computation by Moment Methods*. New York: Macmillan, 1968.

[8] W. H. Press, B. P. Flannery, S. A. Teukolsky, and W. T. Vetterling, *Numerical Recipes in C*. Cambridge: Cambridge Univ. Press, 1988.